Fault-valve behavior estimated from intensive foreshock and aftershock activity in the 2017 M 5.3 Kagoshima Bay, Kyushu, southern Japan, earthquake sequence

Yoshiaki Matsumoto[1+], Keisuke Yoshida[1*], Toru Matsuzawa[1], and Akira Hasegawa[1]

[1] Research Center for Prediction of Earthquakes and Volcanic Eruptions, Graduate School of Science, Tohoku University, Sendai 980, Japan

+ Now at Japan Meteorological Agency, Japan

*Corresponding author: Keisuke Yoshida (keisuke.yoshida.d7@tohoku.ac.jp)

Key Points:

- Intensive foreshock activity exhibits an evident migration behavior on a plane.
- Aftershock hypocenters migrate toward shallower levels using several planes.
- Upward pore pressure migration explains the occurrence of this foreshock-mainshock-aftershock sequence.

Abstract

Fluid migration and pore pressure changes within the Earth are key to understanding earthquake occurrences. In this study, we investigated the spatiotemporal characteristics of intensive foreshock and aftershock activity for the 2017 M_{JMA} 5.3 earthquake in Kagoshima Bay, southern Japan, to examine the physical process governing this earthquake sequence. We determined that foreshock hypocenters moved slowly on a sharply-defined steeply-dipping plane, which probably represents the same plane of the mainshock source fault. The mainshock hypocenter was located at an edge of a seismic gap formed by foreshocks along the plane, suggesting that the mainshock ruptured this seismic gap. Aftershock hypocenters, distributed along several steeply-dipping planes exhibited an overall upward migration. Aftershock activity slightly deviated from a simple mainshock-aftershock type, suggesting the existence of an aseismic process behind this earthquake sequence. We propose a hypothesis that consistently explains these observations. First, fluids rose from the deeper portion and intruded into the fault plane, reduced the fault strength, and caused the foreshock sequence, as well as, possible aseismic slips. An area with a relatively high fault strength on the plane existed, where the mainshock rupture finally occurred due to a continuous decrease in the fault strength associated with increasing pore pressure and an increase in the shear stress associated with the aseismic slip and foreshocks. The change in the pore pressure associated with post-failure fluid discharge contributed to the aftershock activity, causing upward fluid migration. These observations show the importance of fluid movement at depth, when attempting to understand the earthquake cycle.

1. Introduction

Earthquakes are a natural phenomenon wherein a high-speed rupture propagates along a fault. Two factors control the occurrence of an earthquake: an increase in the shear stress acting on the fault and a decrease in the fault strength. Previous studies suggest that an increase in the pore pressure plays an important role in earthquake occurrence (e.g., Hasegawa, 2017; Hubbert & Rubey, 1959; Nur & Booker, 1972; Sibson, 1992; Rice, 1992) because there is a decrease in the fault strength with a rise in the pore pressure.

A well-known example of fluid-driven seismicity is seismicity induced by fluid injection for engineering purposes (e.g., Ellsworth, 2013). There is also growing evidence that the occurrences of numerous natural earthquake swarms are closely related to fluid movements at depth. Yukutake et al. (2011) precisely determine the hypocenters and focal mechanisms of the 2009 Hakone volcano earthquake swarm, suggesting that the diffusion of highly pressured fluid triggered this swarm. Shelly et al. (2016) investigate the spatiotemporal evolution of seismic activity in the Long Valley Caldera, California, suggesting that an evolving pore pressure transient with a low-viscosity fluid initiated and sustained the swarm in 2014. Several earthquake swarms, which occurred after the 2011 Tohoku-Oki earthquake, may have been triggered by a reduction in fault strength due to upward pore pressure migrations (Terakawa et al., 2013; Okada et al., 2015; Yoshida et al., 2016a, 2019a). Many natural seismic swarm activities, including the examples above, have similar characteristics to fluid-injection-induced seismicity, such as the migration behavior of the earthquake hypocenters. This similarity supports the hypothesis that the swarm generation mechanism is essentially identical to fluid-injection-induced seismicity (e.g., Cox, 2016).

Not only earthquake swarms but also foreshock-mainshock-aftershock sequences may be closely-related to fluid behavior in the Earth. Sibson (1992) proposes a model in which the pore pressure cycle controls the earthquake cycle due to over-pressurized fluids that rise from the deeper portion of the fault (i.e., the fault-valve model). In this model, fault ruptures create transient fracture permeability within the fault zone, acting as valves that promote the upward discharge of fluids from deeper portions of the crust. This model is supported by various geological and geophysical observations (Sibson, 2020). Hasegawa et al. (2005) propose a model of the deformation process in a subduction zone based on various geophysical observations, including seismic tomography results, in NE Japan. In this model, fluids expelled from the subducting slab migrate upward, reaches the crust, and causes anelastic deformation of the crust, including earthquakes.

Migration behavior of at hypocenters can be occasionally observed for fluid-injection-induced seismicity and natural earthquake swarms (e.g., Shapiro et al., 1997; Yukutake et al., 2011; Yoshida & Hasegawa, 2018a,b). There are two models that explain earthquake migration: pore pressure migration and aseismic slip propagation. In the first mechanism, the migration of hypocenters is presumed to reflect the migration of fluids (e.g., Shapiro et al., 1997; Talwani et al., 2007). In the second mechanism, hypocenter migration is presumed to be a result of aseismic slip propagation (e.g., Lohman & McGuire, 2007; Roland & McGuire, 2009). Both mechanisms are likely responsible for the observed hypocenter migration behaviors, where the two mechanisms can occasionally coexist (Waite & Smith, 2002; Ross et al., 2017; Yoshida & Hasegawa, 2018; Barros et al., 2020). The space-time distributions of earthquake hypocenters can be estimated more precisely than other seismological parameters, such as the fault slip and seismic velocity. We can extract information on pore pressure migration and aseismic slip

propagation, which is crucial to understand the earthquake generation, by examining precisely-relocated hypocenters.

On Kyushu Island in Southern Japan, the volcanic front formed due to the subduction of the Philippine Sea Plate. Several of the most active volcanoes in Japan are distributed along this volcanic front (e.g., Sakurajima volcano and Aso volcano). Kagoshima Bay is located on this volcanic front, where a low gravity anomaly extends from north to south. On July 11, 2017, an M_{JMA} 5.3 strike-slip earthquake occurred at a depth of approximately 10 km in Kagoshima Bay (Fig. 1). Seismicity had been activated since December 2016 (Fig. 1(c)) near the mainshock hypocenter. For this foreshock activity, 1,843 events were located and listed in the Japan Meteorological Agency (JMA) unified catalogue. Seismicity had been increasingly active since the occurrence of the mainshock, i.e., 12,595 events were recorded in the JMA catalogue. Focal mechanisms of the earthquakes in this region, estimated by the JMA, show a strike-slip type with a NW-SE P-axis (Fig. 1(b)). Nanjo et al. (2018) suggest that fluid movement caused the earthquake sequence in Kagoshima Bay based on the spatiotemporal variation in the b-value and the migration behavior of the hypocenters.

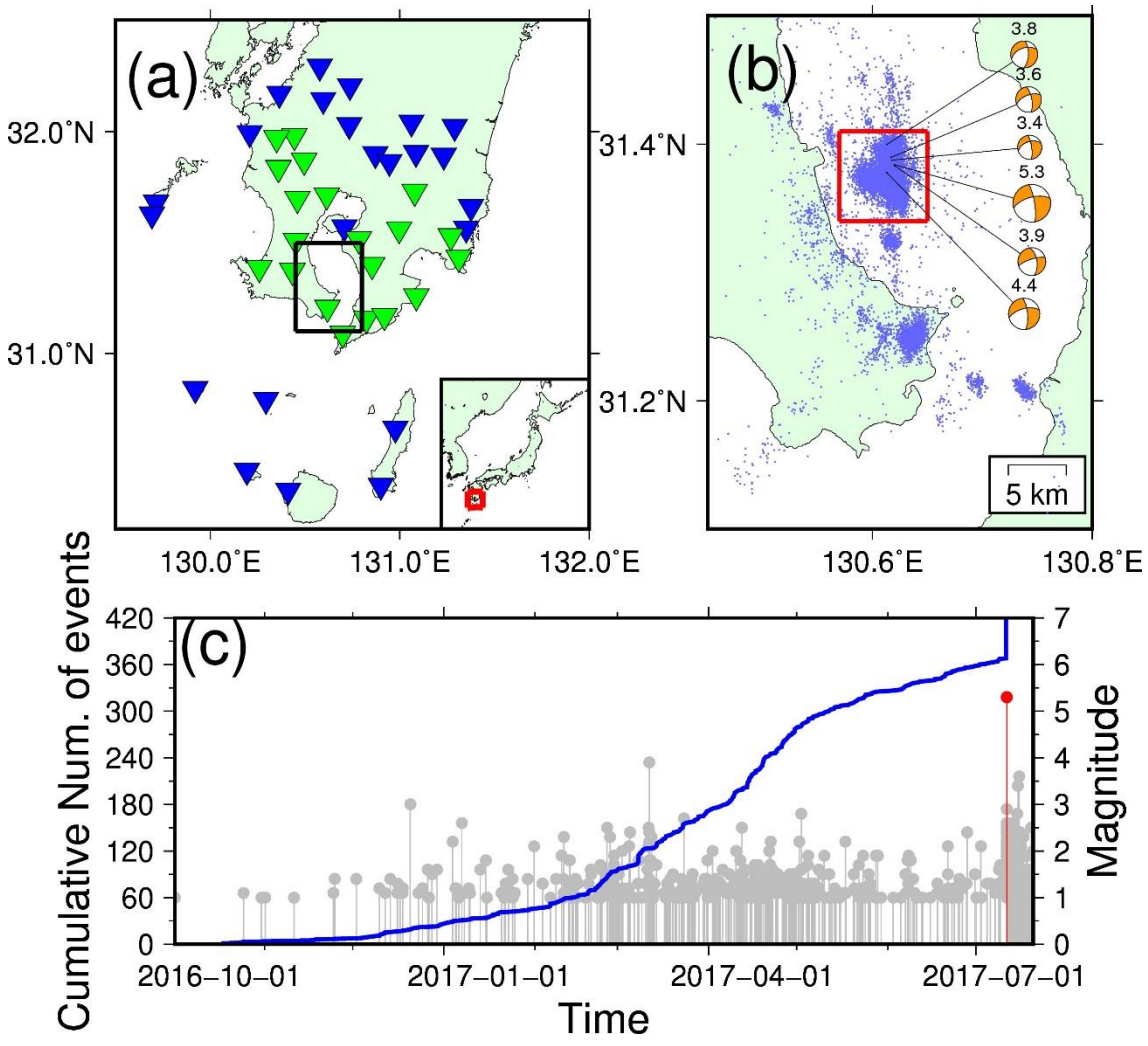

Figure 1. (a) A map showing southern Kyushu. Inverted triangles indicate the seismic stations. We used picked arrival time data obtained at stations in both blue and green. We analyzed

waveform data obtained at stations in green. The black square shows the target area of this study. (b) Hypocenter distribution of earthquakes that occurred in Kagoshima Bay from January 1, 2010, to April 8, 2018, and their focal mechanisms. Hypocenters and focal mechanisms were taken from the JMA unified catalog. The red square is defined as "the area around the mainshock hypocenter" in this study. The numbers at the tops of the focal mechanisms indicate the JMA magnitude of each earthquake. (c) M-T diagram and cumulative number of $M_{JMA} \geq 1.0$ *earthquakes that occurred in the area surrounding the mainshock hypocenter (i.e., the red square in Fig. 1(b)) prior to the mainshock. The vertical red line denotes the mainshock.*

In this study, we examine, in detail, the physical process behind the M_{JMA} 5.3 Kagoshima Bay earthquake sequence in Kyushu, southern Japan. First, we precisely determine the hypocenters and focal mechanisms of this earthquake sequence, as well as delineating the fault structure. We also estimate the source size of the mainshock and examine its relationship with the foreshocks and aftershocks to obtain a comprehensive view of this foreshock-mainshock-aftershock sequence. We then examine the spatiotemporal characteristics of the intensive foreshock and aftershock activity to extract information on the aseismic phenomena behind this earthquake sequence. Finally, by integrating the obtained observations, we propose a model that can explain the occurrence and characteristics of the foreshock-mainshock-aftershock sequence associated with the 2017 M5.3 Kagoshima Bay earthquake.

2. Methods

2.1. Hypocenter relocations

We relocated 18,390 events listed in the JMA unified catalogue in the southern Kagoshima Bay region for the period from January 1, 2010, to April 8, 2018, using the Double-Difference method (Waldhauser & Ellsworth, 2000). This relative relocation method minimizes the residuals between the observed and theoretical travel time differences for adjacent earthquake pairs at each station. We applied the Double-Difference method to the differential arrival time data, which were precisely estimated from the waveform cross-correlation, and those listed in the JMA unified catalog. The procedure is essentially identical to that reported in Yoshida and Hasegawa (2018a,b), which is briefly described as follows.

First, we obtained precise differential arrival time data using waveform cross-correlations. We used the waveform data observed at 20 permanent seismic stations that surround the focal area (Fig. 1(a); green stations). At each station, the ground velocity is measured by three-component short-period seismometers (natural period of 1s) and recorded at a 100 Hz sampling rate. We applied a 5–12 Hz Butterworth filter to the waveforms of each target event obtained at each seismic station. We used 2.8 s and 4.3 s time windows for the P- and S-waves, respectively, beginning 0.3 s before the arrival times. Here, arrival times in the JMA unified catalogue were used when listed. Otherwise, arrival times were estimated based on the 1-D velocity model, i.e., JMA2001 (Ueno et al., 2002), and the hypocenters and origin times listed in the JMA unified catalogue. We calculated waveform cross-correlations of the event pairs, whose hypocenters were located within 3 km of each other, and obtained the differential arrival times when the cross-correlation coefficients were greater than 0.8. As a result, we acquired 23,077,393 P-wave differential arrival time data and 37,128,628 S-wave data. We also derived the differential arrival data from the arrival time data listed in the JMA unified catalog: 411,421 for P-wave and 467,687 for S-wave. For the mainshock, only data derived from the JMA unified catalog were used due to its long source duration.

Second, we applied the hypo-DD algorithm (Waldhauser, 2001) to the differential arrival time data. We used a spherical shell two-layer model (Aki, 1965) for hypocenter relocation. In this model, seismic velocities vary in each layer in proportion to the power of the distance from the center of the Earth (Fig. S1). The medium parameters were determined for consistency with seismic tomography results of the Kyushu region (Saiga et al., 2010). We used the hypocenters listed in the JMA unified catalogue for the initial locations for the relocation. Figure 2 shows the distribution of these initial hypocenters. Differential arrival time data were weighted in proportion to the square root of a cross-correlation coefficient. Hypocenters were updated during 50 iterations of the relocation procedure. In the first 10 iterations, we gave more weight to the catalogue data to constrain the relative locations with a large scale. In the latter 40 iterations, more weight was given to the data derived by the cross correlations to delineate shorter scale features.

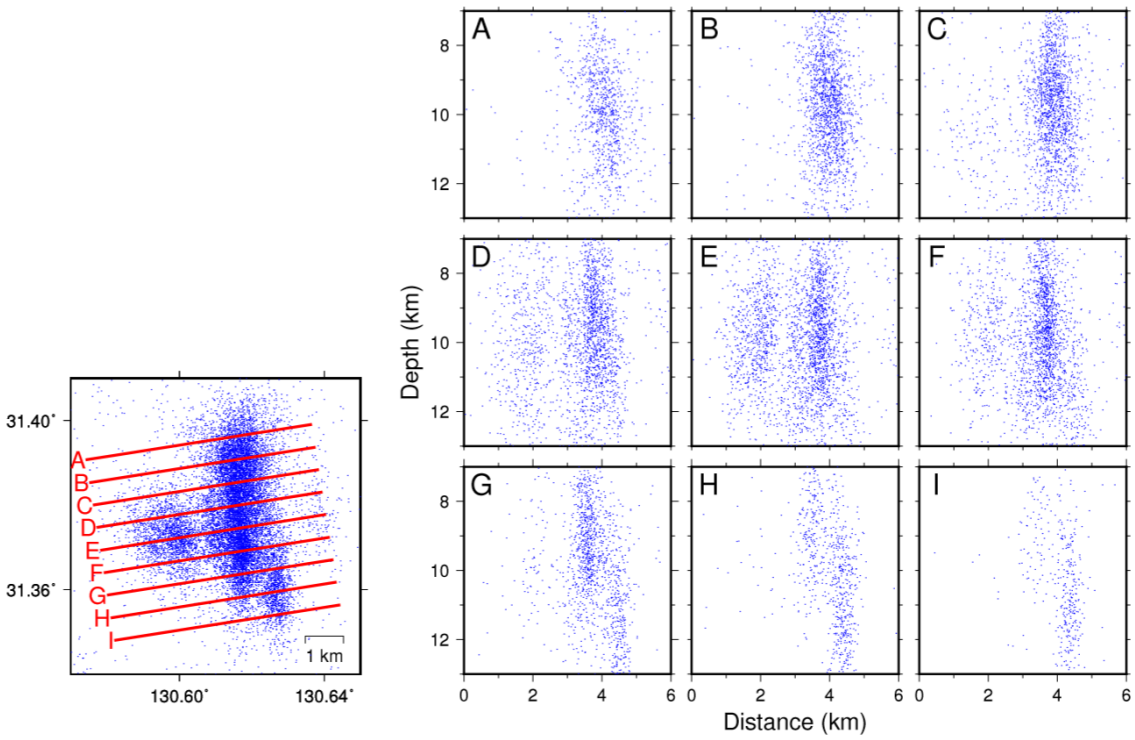

Figure 2. The distribution of the initial hypocenters listed in the JMA unified catalog. Blue dots indicate the locations of the hypocenters. The left figure is a map view while the right nine figures are the cross-sectional views along vertical sections indicated by the red lines from A to I in the left figure.

2.2. Estimation of focal mechanisms

We estimated the focal mechanisms based on the amplitude ratios of the waveforms using the method of Yoshida et al. (2019b) after Dahm (1996). We used six focal mechanisms determined by the JMA (Fig. 1(b)) for reference to the correct path- and site-effects on the waveform. We attempted to determine the focal mechanisms of 161 earthquakes with $M_{JMA} \geq 2$. We used displacement waveforms obtained by integrating the velocity waveform records over time at the 20 stations (green triangles in Fig. 1(a)) surrounding the hypocenters. The vertical component was used for the analysis of the P-wave while radial and transverse components were used for that of the S-wave. We applied a 2–5 Hz band-pass filter to the waveforms, cutting them out with time windows of 2.8 s for P-waves and 4.3 s for S-waves beginning 0.3 s before the arrival times.

We used waveform cross-correlations to measure the amplitude ratios between a target event and reference event. The amplitude ratios were obtained for the pairs when the absolute value of the correlation coefficient was higher than 0.75. We used principal component analysis (PCA) to measure the amplitude ratios.

We only estimated the mechanism solution when the amplitude ratios were obtained for more than 20 channels. We eliminated results for V.R. (Variance Reduction) less than 80 as follows:

$$\text{V.R.} = \left(1 - \frac{\sum_{k=1}^{n}(d_k - s_k)^2}{\sum_{k=1}^{n} d_k^2}\right) \cdot 100, \quad \#(1)$$

where d_k and s_k are the observed and calculated displacement amplitude ratios, respectively, at channel k.

2.3. Estimation of mainshock source size

We estimated the source size of the mainshock based on the circular-crack source model (e.g., Sato & Hirasawa, 1973; Madariaga, 1976). In these source models, the source radius is related to the S-wave corner frequency, f_c, as follows:

$$r = \frac{k\beta}{f_c}, \#(2)$$

where r is the source radius, k is a constant, and β is the S-wave velocity near the source. Assuming a rupture velocity of 0.9β, k is 0.44 in the model of Sato and Hirasawa (1973) and 0.32 in the model of Madariaga (1976) for P-waves. As the estimated source size depends on the adopted source model, we computed the fault size using both models. We assumed β = 3.4 km/s.

We used the spectral ratio method (e.g., Imanishi & Ellsworth, 2006) to estimate the corner frequency of the mainshock. In this method, propagation- and site-effects on the seismic wave are empirically removed using the waveforms of an adjacent small earthquake (EGF event). Assuming that the source spectrum, i.e., $S_j(f)$, follows the ω^2 model (Aki, 1967; Brune, 1970), the theoretical ratio between the velocity spectra of the mainshock, $v_i(f)$, and the EGF event, $v_i^{egf}(f)$, at station-i is as follows:

$$SSR_{ij}(f) = \frac{v_i(f)}{v_i^{egf}(f)} = \frac{M_0}{M_0^{egf}} \frac{R_{\theta\varphi i}}{R_{\theta\varphi i}^{egf}} \frac{1 + \left(\frac{f}{f_c^{egf}}\right)^2}{1 + \left(\frac{f}{f_c}\right)^2} \#(3)$$

,

where M_0 and M_0^{egf} are the seismic moments of the target earthquake and EGF event, respectively, $R_{\theta\varphi ij}$ and $R_{\theta\varphi i}^{egf}$ are their radiation patterns at station i, respectively, and f_c^{egf} is the corner frequency of the EGF event. Based on Eq. (3), we can estimate f_c from the shape of the spectral ratios.

We calculated spectral ratios using observed P-wave velocity waveforms at the 20 stations surrounding the source area (green inverted triangles in Fig. 1(b)). The EGF events were earthquakes with M ≥ 2, whose distance from the mainshock was < 1.0 km based on the relocated hypocenters. The procedure was performed as follows with reference to Yoshida et al. (2017):

(1) For the target mainshock and EGF events, waveforms of the three components were cut out for a 2.0 s time window starting 0.3 s before the arrival time of the P-wave at each station. The multitaper method (Thomson, 1982; Prieto et al., 2009) was applied to calculate the spectra.

(2) For the channels where the EGF observation spectrum always satisfied S/N > 2 in the frequency range of 0.5–30.0 Hz, the spectral ratio was calculated between the mainshock and EGF event. Here, we used waveforms up to 0.3 s before the arrival time of the P-waves for the noise window.

(3) We calculated the geometric mean of the spectral ratios $GSR(f)$ of all the channels at each frequency point for the EGF events, which satisfied the above criterion at 5 or more stations as follows:

$$GSR(f) = \prod_{i=1}^{N} \left(SR_i(f)\right)^{\frac{1}{N}}, \#(4)$$

where $SR_i(f)$ is the observed spectral ratios obtained at station$i$ and N is the number of stations.

(4) Using the grid search, the corner frequencies of the mainshock, f_c, and EGF event, f_c^{egf}, were determined by minimizing the following evaluation function, J:

$$J = \sum_{k=1}^{n_{freq}} \left|\log\left(GSR(f_k)\right) - A\log\left(NSR\left(f_k; f_c, f_c^{egf}\right)\right)\right| \#(5)$$

where $NSR\left(f; f_c, f_c^{egf}\right) = \frac{1+(f/f_c^{egf})^2}{1+(f/f_c)^2}$, n_{freq} is the number of frequency points and f_k is frequency point at 0.5 Hz intervals from 0.5 to 30 Hz. The grid search was performed for f_c and f_c^{egf} while assuming a range from 0.1 to 100 Hz at 0.1-Hz-steps. The amplitude ratio, A, was estimated using the least squares method at each grid-search step.

We applied the spectral ratio method to 33 EGF candidates. As a result, we obtained spectral ratios from 21 EGF events, which satisfy our criteria for the S/N ratio and data number. Figure S2 shows the spectral ratios from the 21 EGF events.

2.4. Detection of aseismic process from seismicity

Previous studies have reported that seismic activity caused by external forces, such as fluid movements or aseismic slips, has different characteristics from the mainshock-aftershock sequence type (e.g., Hainzl & Ogata, 2005; Roland & McGuire, 2009; Kumazawa & Ogata, 2013; Yoshida & Hasegawa, 2018b). This suggests that investigating seismicity may provide clues to the aseismic processes behind the occurrences of earthquakes.

The Epidemic Type Aftershock Sequence (ETAS) model (Ogata, 1988), based on the superposition of the modified Omori law (Ustu, 1961), can appropriately explain mainshock-aftershock seismicity. The ETAS model assumes that the seismicity rate is a summation of the background rate of independent events, λ_0, and aftershocks triggered by each event, $\lambda_i(t)$, as follows:

$$\lambda(t) = \lambda_0 + \sum_{i:t_i<t} \lambda_i(t) \#(6)$$

.

Each earthquake can trigger its own aftershock sequence following the modified Omori Law (Utsu et al., 1995) as follows:

$$\Lambda_i(t) = \frac{K_0}{(c+t-t_i)^p} e^{\alpha(M_i - M_{\min})} \#(7)$$

,

where t_i is the occurrence time; M_i is the magnitude of each event, $-i$, that occurred prior to time t; $M_{\min}$ is the magnitude of completeness of the earthquake catalogue; K_0, c, and p are constants; and t is the elapsed time since the main event.

We applied the ETAS model to the seismicity observed after the mainshock in Kagoshima Bay and investigated the difference between the simulated and observed seismicity. We found that the foreshock activity cannot be explained by the ETAS model, which is likely because the aseismic process mainly controlled the foreshock activity. We used the timings and magnitudes of the earthquakes listed in the JMA catalogue. The lower limit of magnitude, M_C, was set to 1.0. Figure S3 shows the magnitude-frequency distribution. The distribution appears to follow the Gutenberg-Richter law (Gutenberg & Richter, 1944) when $M_{JMA} \geq 1.0$. The SASeis2006 algorithm by Ogata (2006) was used for model parameter estimation and residual analysis in the ETAS model.

3. Results

3.1. Fault structure and seismic gap

We obtained the relocated hypocenters of 18,211 events and focal mechanisms of 61 events. Nearly all the events in the Kagoshima-Bay earthquake sequence can be precisely relocated by the Double-Difference algorithm. Location data for 179 earthquakes were removed because their hypocenters were located above the ground surface or they included outliers in the differential arrival time data.

Figure 3 shows the distribution of relocated hypocenters. Most hypocenters were located within ~5 km from the mainshock hypocenter and distributed along several planes. This characteristic is in contrast to the distribution of the initial hypocenters (Fig. 2), which were scattered three-dimensionally similar to a cloud. This drastic change in the hypocenter distribution derives from the improvements to the relative locations of the hypocenters in this study due to numerous and precise differential arrival time data. Such dramatic improvements to the relative hypocenters for the shallow earthquakes, from a cloud-like distribution to planar structures, were also reported in previous studies from Japan based on a similar method (e.g., Yoshida & Hasegawa, 2018a,b). The cloud-like distribution of the initial hypocenters actually reflects the determination error of hypocenter locations in the JMA unified catalog due to errors in manual picking.

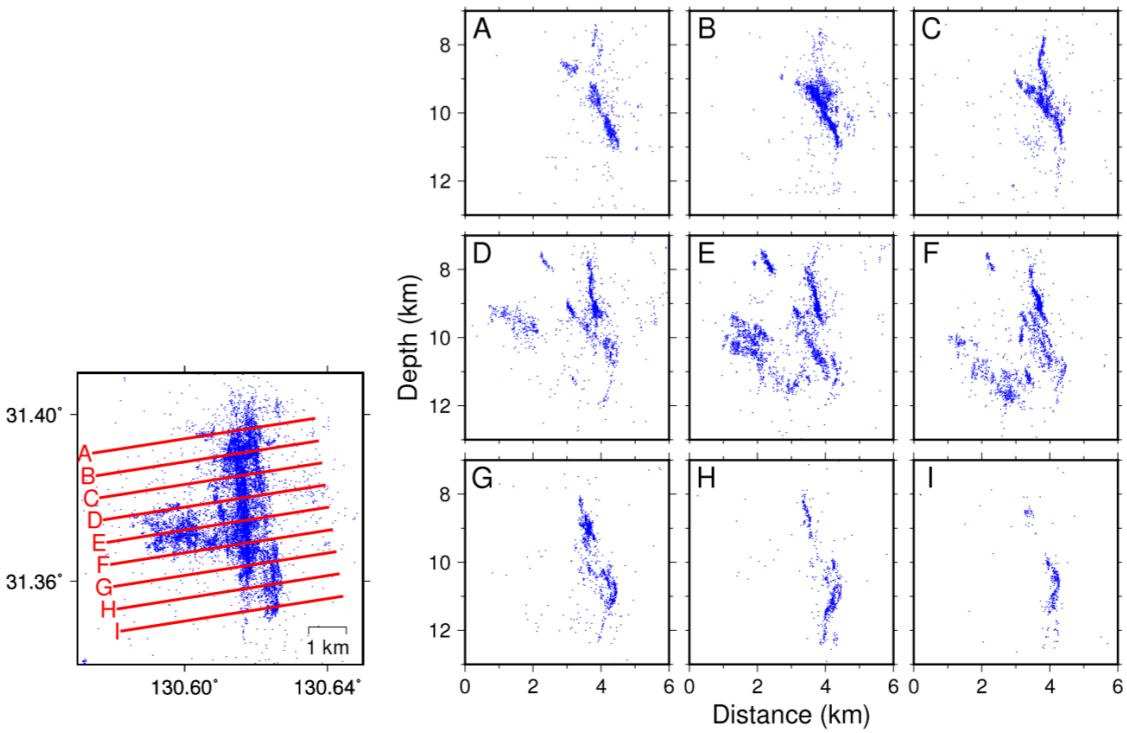

Figure 3. Distribution of the relocated hypocenters based on the DD method. Blue dots indicate the locations of the hypocenters. The left panel is a map view while the right nine figures (A–I) are the cross-sectional views along the vertical sections indicated by the red lines from A to I in the left figure.

Figure 4 shows the spatial distribution of the focal mechanisms. As the reference focal mechanisms are located in the northern part of the source region (Fig. 1(b)), newly-estimated focal mechanisms are mainly located in the northern part. We can observe that the nodal planes for most focal mechanisms are parallel to the planar structures of the hypocenters, suggesting that these individual small earthquakes occurred on several macroscopic planes.

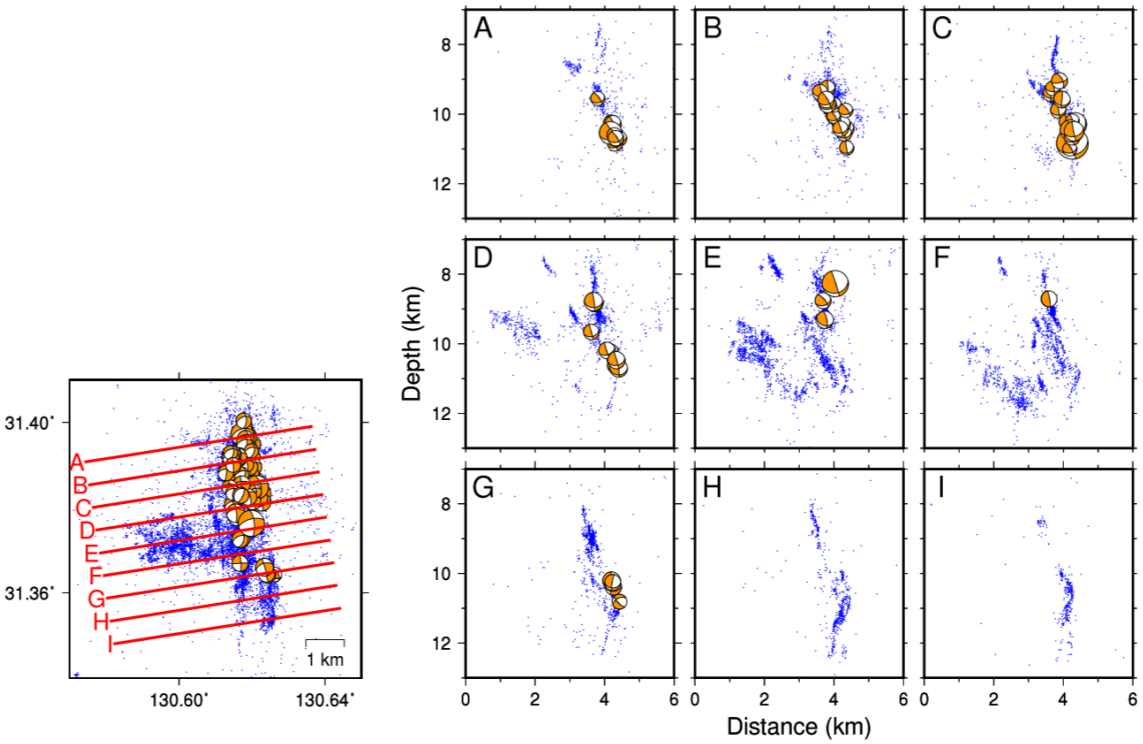

Figure 4. The estimated focal mechanisms plotted on the hypocenter distribution. The left figure is a map view and the right nine figures (A–I) are cross-sectional views along vertical sections indicated by the red lines from A to I in the left figure.

Based on Figs. 3 and 4, the fault structures of the 2017 Kagoshima Bay earthquake sequence appear to be quite complex, consisting of several subparallel planes. However, the distribution of hypocenters was relatively simple before the mainshock. Figure 5 shows the spatial distribution of hypocenters with respect to the foreshock activity. Most hypocenters are neatly distributed on one plane with the strike parallel to ones of the nodal planes of the focal mechanisms in the mainshock and individual small earthquakes, suggesting that most foreshocks and the mainshock occurred on this plane.

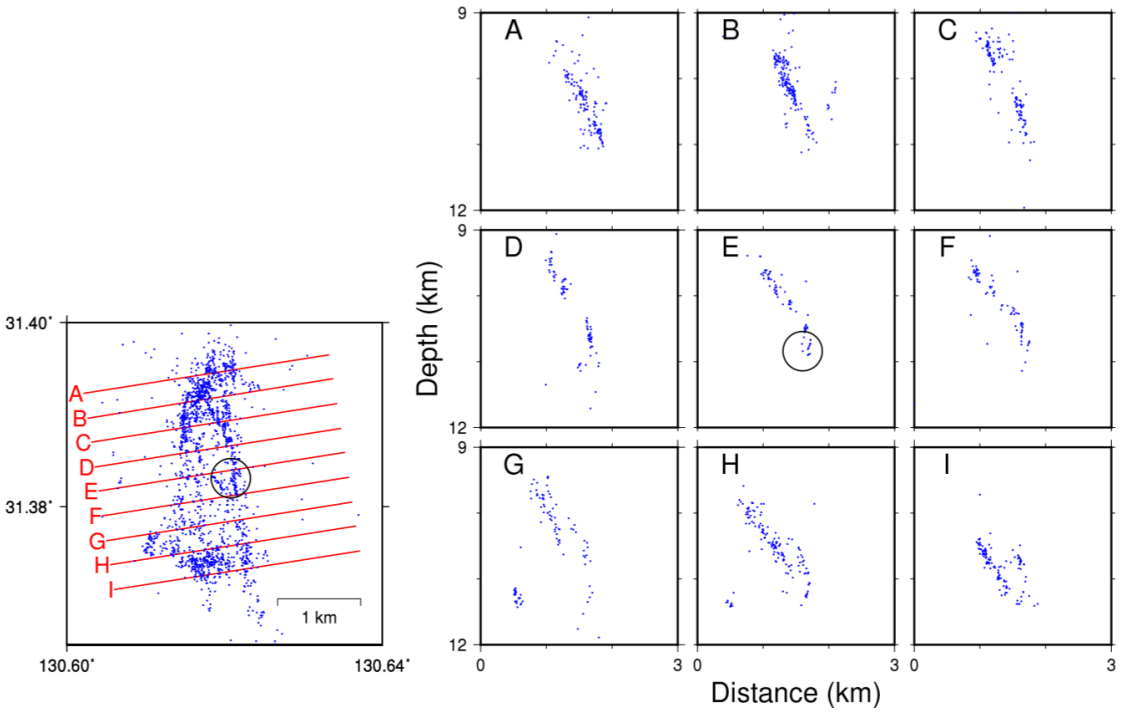

Figure 5. The hypocenter distribution of the foreshock activity. The left panel is a map view. The right nine figures (A–I) show the hypocenters projected onto the vertical sections on the red lines from A to I in the left panel. The large black circle indicates the hypocenter location of the mainshock.

The hypocenters of the foreshock activity are not uniformly distributed on this plane, but are distributed in a doughnut shape to avoid the center of the plane forming a seismic gap. The hypocenter of the mainshock is located at an edge of this seismic gap. Figure S4 compares the hypocenters of the foreshocks to those of the aftershocks. Although the aftershocks appear to occur inside the seismic gap based on the map-view, they actually occurred in a portion shallower than the foreshocks. Aftershocks also avoided any occurrences in the seismic gap of the foreshock activity.

This doughnut-like pattern in the foreshocks is similar to what is known as the “Mogi doughnut” (Mogi, 1969). Aftershocks have also been reported to have avoided occurrences along the segment with the rupture of the mainshock (e.g., Mendoza & Hartzell, 1988; Das & Henry, 2003; Woessner et al., 2006; Asano et al., 2011; Ebel & Chambers, 2016; Yoshida et al., 2016b; Ross et al., 2017 & 2018; Wetzler et al., 2018) likely because the mainshock released the shear stress at this point. Therefore, the mainshock rupture of the Kagoshima Bay earthquake sequence may have mainly occurred in this seismic gap. The median value of the estimated corner frequencies of the mainshock was 2.1 Hz (Fig. S2). The first and third quartiles were 1.9 and 2.5 Hz, respectively. Based on the median corner frequency, the source radius of the mainshock is 710 m according to the model proposed in Sato and Hirasawa (1973) and 520m using the model proposed in Madariaga (1976). In Fig. S5, the size of the seismic gap was compared with the estimated fault size of the mainshock. The fault size of the mainshock falls within the seismic gap. This is consistent with our estimation that the mainshock rupture occurred in the seismic gap of the foreshock and aftershock activities. A similar spatial separation in the rupture area of

the mainshock with the foreshock and aftershock activities was also reported for a recent M5.2 intraplate earthquake in Akita, NE Japan (Yoshida et al., 2020).

3.2. Foreshocks and aftershock migration behaviors

Figure 6 shows the occurrence timings of the foreshock activity based on a color scale. Foreshocks were mainly located in the northern part at the beginning, but gradually moved toward the southern part. Figure 7a, 7b, and 7c compare the occurrence timing of each earthquake with the longitude, latitude, and depth, respectively, which illustrate the migration behavior. In the longitudinal direction (Fig. 7a), the hypocenters expanded nearly symmetrically in the first 230 days of foreshock activity, concentrating on the east side, i.e., the location of the mainshock hypocenter during the last ~70 days of activity. In the latitudinal direction (Fig. 7b), the hypocenters evidently migrated from the north to the south. In the depth direction (Fig. 7c), the hypocenters migrated both in the shallow and deep directions, such that most earthquakes occurred in the deeper part, i.e., the location of the mainshock hypocenter during the last ~70 days of activity.

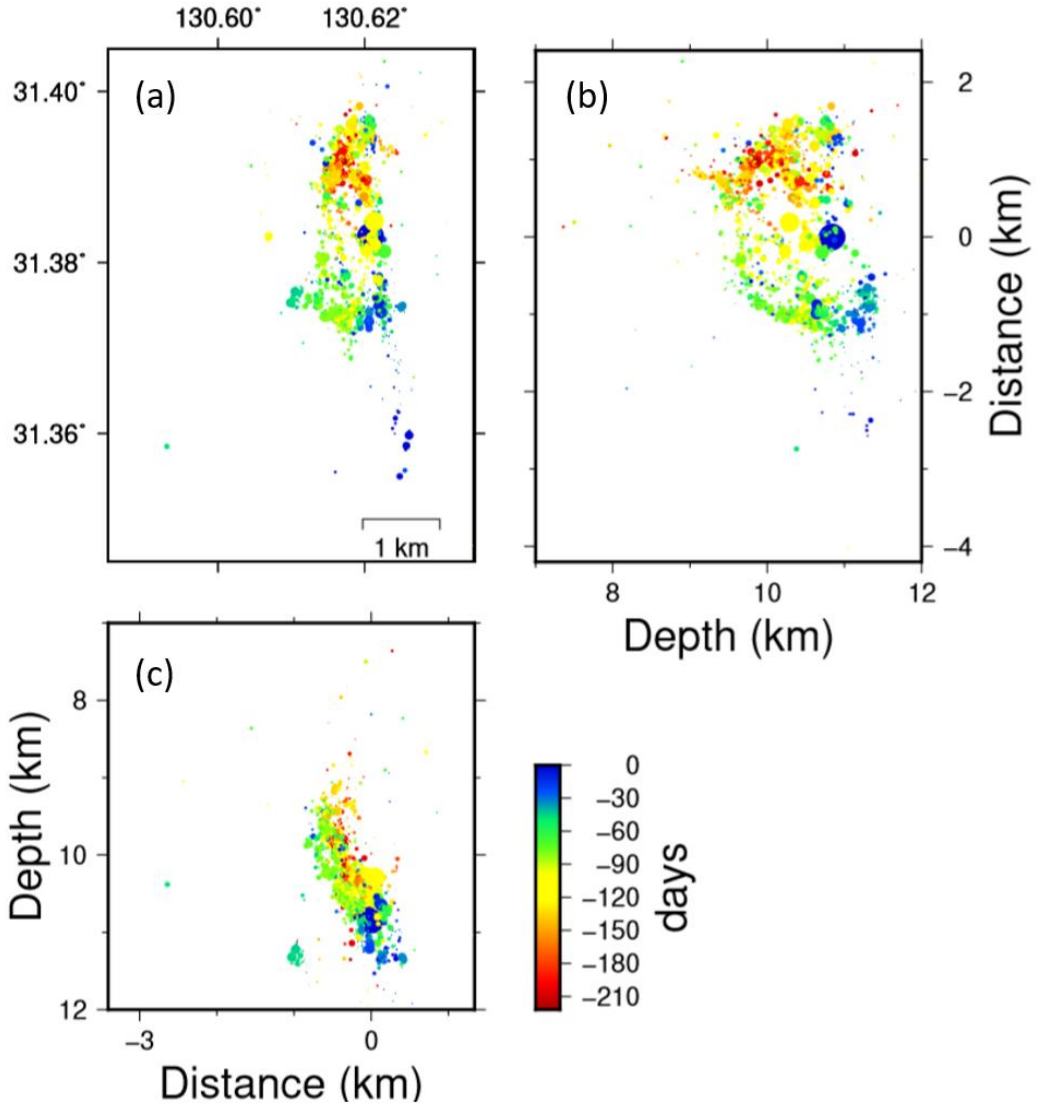

Figure 6. Spatiotemporal evolution of the hypocenters as a function of the foreshock activity. The hypocenters projected onto (a) the map view, (b) the north–south vertical cross-section, and (c) the east–west vertical cross-section, where the symbol sizes correspond to the JMA magnitudes. The hypocenters are colored according to the occurrence time measured relative to that of the mainshock, i.e., the mainshock as time 0, with negative days denoting hypocenters before the mainshock.

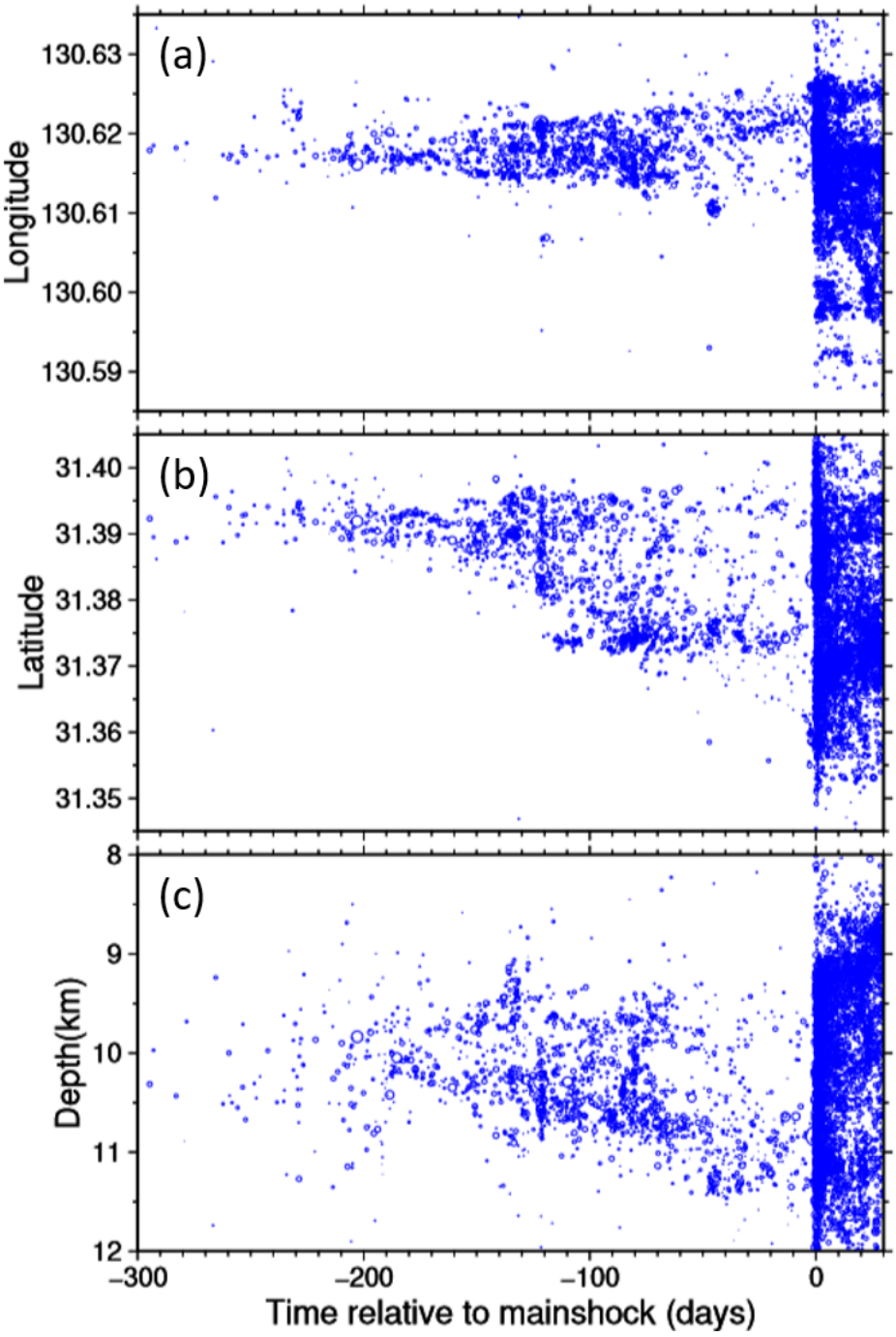

Figure 7. Temporal evolution of hypocenters in the (a) latitude, (b) longitude, and (c) depth directions. The circle size corresponds to the JMA magnitude.

Figure 8 shows the distribution of aftershock hypocenters colored by the occurrence time of each event. Figure 9 shows the temporal evolution of the aftershock hypocenters as a function of the depth. Furthermore, Fig. S3 shows the temporal evolution of the aftershock hypocenters in both the latitudinal and longitudinal directions. As the spatial distribution of the aftershocks is complex, the spatiotemporal features of the aftershock activity are more difficult to examine than that of the foreshock activity. Overall, the aftershock hypocenters moved upward with time as shown in Fig. 9, which depicts the depths above which the shallowest 5% of the hypocenters are located (D05), where each bin contains 400 events, as denoted by the red curve. Although earthquakes occurred in a relatively deep region immediately after the mainshock, the upper limit of the seismic depth (D05) gradually expanded in the shallow direction, i.e., the hypocenters gradually moved to the shallower part with time after the mainshock.

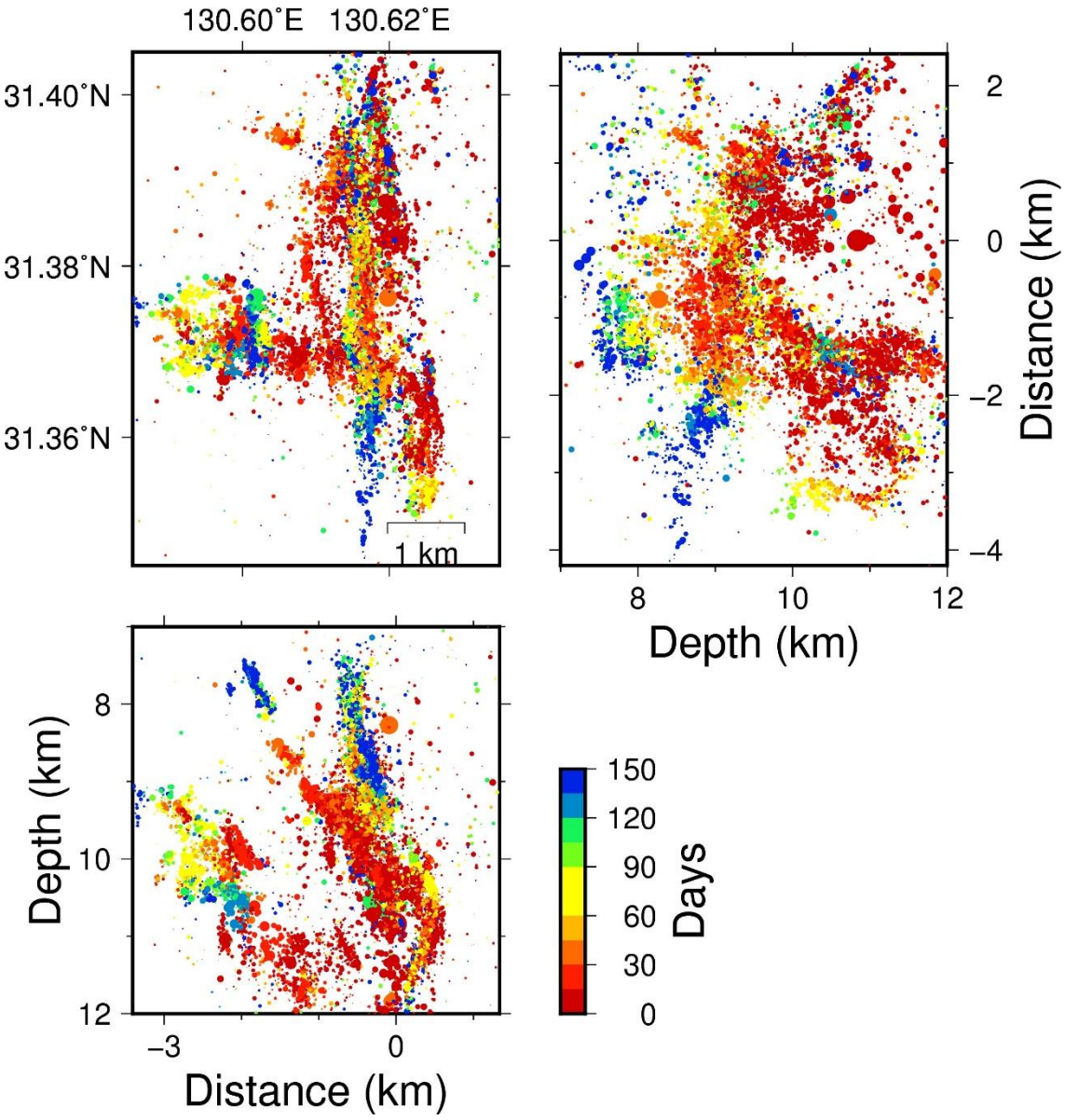

Figure 8. Spatiotemporal evolution of the aftershock hypocenters. The hypocenters projected onto the (a) map view, (b) north–south vertical cross-section, and (c) east–west vertical cross-section, shown by circles with sizes corresponding to the JMA magnitude. The hypocenters have specific colors based on the occurrence time measured from that of the mainshock.

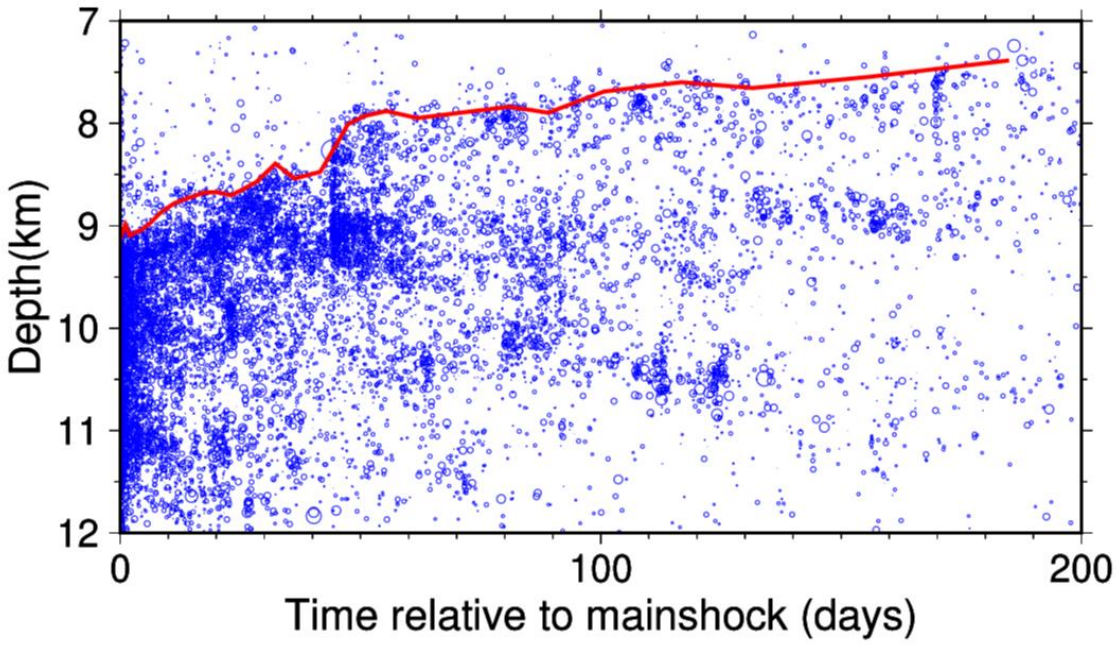

Figure 9. The temporal evolution of the aftershock hypocenters in the depth direction. Circle size corresponds to the JMA magnitude. The red line indicates the depth above which the shallowest 5% of the hypocenters are located (D05) at every bin with 400 events in order of occurrence time.

3.3. Seismicity deviation from Omori's law

We investigated the seismicity rate of the Kagoshima Bay earthquake sequence after the mainshock. Figure 10 shows the seismicity rate of the $M_{JMA} \geq 1.0$ events in the area around the mainshock hypocenter (red frame in Fig. 1(b)). The seismic rate was obtained by calculating the reciprocal of the time required to generate ten earthquakes arranged in chronological order. According to Fig. 10, the seismicity rate decreased by a power of the elapsed time immediately after the mainshock, as described by the modified Omori law. We observe that the seismicity rate abruptly increased ~44 days after the mainshock, which corresponds to the occurrence of the largest aftershock at M_{JMA} 4.4, suggesting an increase due to secondary aftershocks. Also, there a high-seismicity-rate period appears from approximately 20 to 40 days after the mainshock, during which the seismic activity is temporarily high despite no large aftershocks.

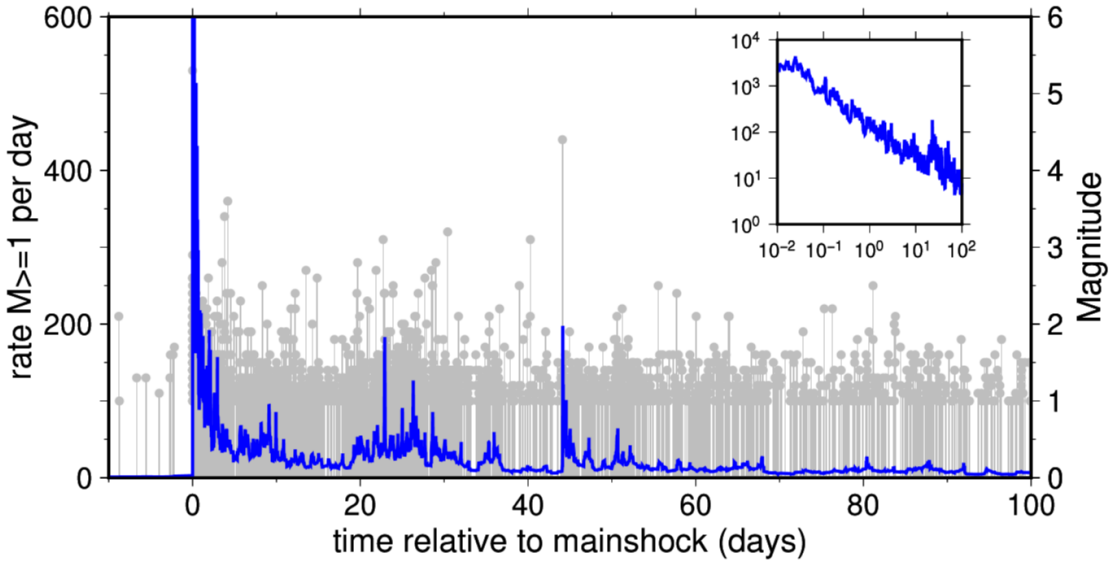

Figure 10. Aftershock occurrence rate of the $M_{JMA} \geq 1.0$ events (blue) and the M-T diagram (gray). Inset compares the aftershock occurrence rate with time on a log-log scale. The occurrence rate was estimated by calculating the reciprocal of the time when 10 events occurred with $M_{JMA} \geq 1.0$.

As a result of the maximum likelihood estimation, the ETAS model parameters were estimated as $K_0 = 45.479$, $c = 0.85120 \times 10^{-2}$, $p = 0.97934$, $\alpha = 1.6096$, and $\mu = 0.18287 \times 10^{-13}$. According to Ogata (1992), the range of α-values is [0.35, 0.85] for swarm seismicity and [1.2, 3.1] for non-swarm seismicity. For the seismic activity in Kagoshima Bay, the estimated α value was within the latter range.

Figure 11 compares the cumulative number of earthquakes simulated from the estimated model parameters with its observed counterpart. The number predicted based on the ETAS model appears to sufficiently explain the overall observed trend. However, the simulated number of earthquakes is apparently lower than the observed number for the period from 20 to 40 days after the mainshock. To quantitatively examine the degree of discrepancy between the model and observation, we performed a residual analysis using the transformed time, similar to Ogata (1988). Figure 11c shows that the discrepancy between the model and observation began to increase at the transformed time of approximately 1,000, which corresponds to approximately 20 days after the mainshock. This difference exceeded the 99% significance level assuming a uniform distribution.

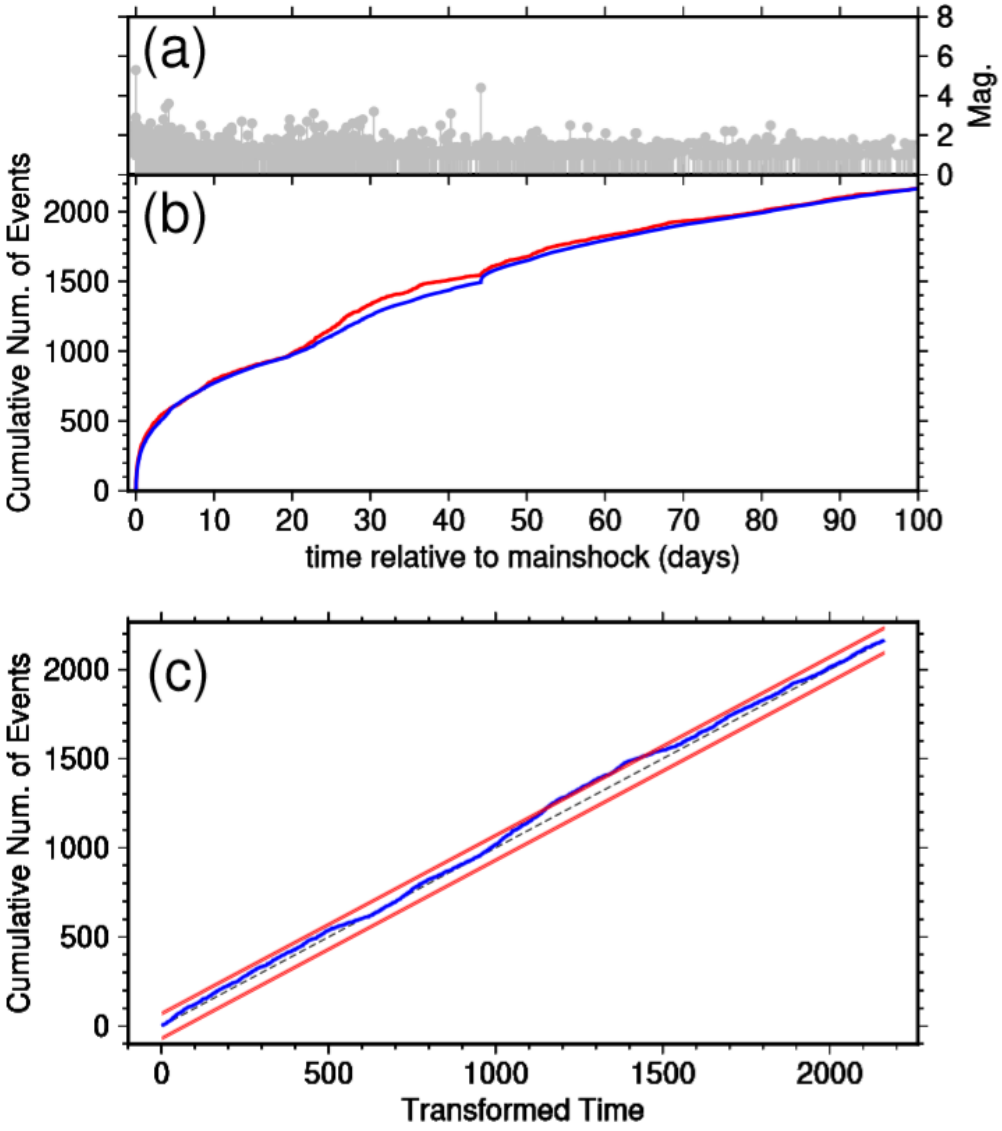

Figure 11. (a) The M-T diagram. (b) Observed cumulative number of aftershocks with $M_{JMA} \geq 1.0$ *(red solid line) and predicted number based on the estimated ETAS parameters (blue solid line). Each represents the cumulative numbers from 0.1 day after the mainshock. (c) Results of the residual analysis, where the blue solid line shows the observed events with respect to the Transformed Time on the horizontal axis and cumulative number of observed* $M_{JMA} \geq 1.0$ *earthquakes on the vertical axis. The black dotted line represents the Transformed Time when the assumed model can entirely explain the observation. The red solid lines indicate the two-sided 95 and 99% error bounds of the Kolmogorov- Smirnov statistic.*

The large discrepancy between the predicted and observed seismicity rates from 20 to 40 days (~1,000–1,500 in Fig. 11(c)) after the mainshock can be understood as temporary increases in the background seismic activity, which was assumed to be constant over the entire period of this analysis. The transient increase in the background seismicity rate suggests that the

Kagoshima Bay earthquake sequence may have been affected by physical processes other than interseismic interactions, especially during this period. During this period, the aftershock hypocenters rapidly migrated upward (Fig. S7). On the other hand, most aftershocks can be explained as general mainshock-aftershock seismic activity, likely suggesting that stress changes caused by the mainshock resulted in numerous aftershocks.

4. Discussion

Our results show that: (1) foreshocks in the 2017 M5.3 Kagoshima Bay earthquake sequence occurred on a single plane steeply inclined to the east while aftershocks occurred on several more complex planar structures, (2) the foreshock hypocenters form a seismic gap, whose size is comparable to the source size of the mainshock, and (3) the foreshock and aftershock hypocenters exhibit clear migration behaviors. In this section, we attempt to integrate these observations and propose a simple model that can explain the occurrence of the foreshock-mainshock-aftershock sequence of the 2017 M5.3 Kagoshima Bay earthquake based on upward fluid movement, which is similar to the model proposed by Sibson (1992).

4.1. Migration of foreshock activity along a plane

Possible causes of hypocenter migration are aseismic processes, such as fluid movement (e.g., Talwani & Acree, 1985; Shapiro et al., 1997) and aseismic slip (e.g., Lohman & McGuire, 2007; Roland & McGuire, 2009). The observed migration behaviors suggest that such aseismic processes played important roles in the generation of the earthquake sequence in Kagoshima Bay.

Figure 12 compares the distances of the foreshock hypocenters from the first event with time. We also show, in Fig. 12, the expansion front of the pore pressure diffusion model reported in Shapiro et al. (1997), represented by the following formula with various diffusion coefficients D_h:

$$r = \sqrt{4\pi D_{\mathrm{h}} t}, \#(9)$$

where r is the distance from the point pressure source and t is time. Here, we set the initiation time to 220 days before the mainshock because the seismicity rate significantly increased at this time (Fig. 1c). We also show the propagation fronts of the linearly-spreading model, which previous studies have occasionally assumed for aseismic slip propagation (e.g., Vidale & Shearer, 2006).

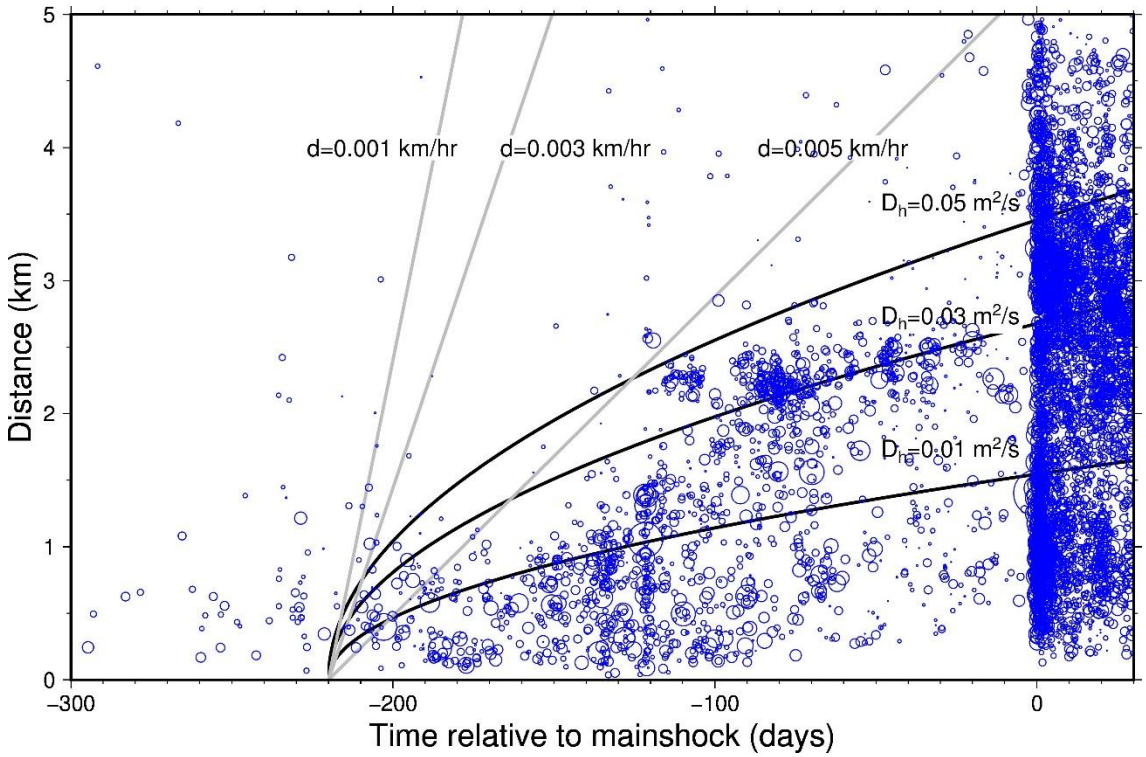

Figure 12. The temporal evolution of the distances between the foreshock activity and the initial hypocenter. Blue circles represent the hypocenters expressed by the size corresponding to the JMA magnitudes. The black curves show the fluid diffusion models with Dh = 0.01, 0.03, and 0.05 m^2/s. Gray straight lines show the linear spreading model with migration speeds of d=0.001, 0.003, and 0.005 km/hr.

We can observe that the pore pressure diffusion model yields a better fit to the observation than the linear spreading model when the hydraulic diffusion coefficient is approximately 0.05 m^2/s. Previous studies have estimated the hydraulic diffusion coefficients in the crust to range from ~0.01–10 m^2/s (e.g., Talwani et al., 2007; Shelly et al., 2016; Yoshida & Hasegawa, 2018a), which is similar to the foreshock migration speed of the M5.3 Kagoshima Bay earthquake sequence. If we assume the linear spreading model, the propagation velocity is approximately 0.001–0.005 km/h. Previous studies have obtained a range of migration speeds for aseismic slip propagations from 0.1–1.0 km/h (e.g., Lohman & McGuire, 2007; Kato et al., 2016), which is significantly higher than the migration speed of the present foreshock activity. If we advance the initiation timing of propagation, the propagation speed becomes even slower. Thus, according to the migration speed and spatiotemporal pattern of foreshocks, the pore pressure diffusion model is more appropriate for explaining the overall migration of the foreshock hypocenters.

Recent observations of fluid-injection-induced seismicity and natural earthquake swarms, however, suggest that an increase in the pore pressure can also trigger aseismic slips (Cornet et al., 1997; Guglielmi et al., 2015; Yoshida & Hasegawa, 2018a; Barros et al., 2020). In the presence of fluids, there is a decrease in the effective normal stress and an increase in the critical nucleation size, such that the occurrence of aseismic slip may be a more likely phenomena (e.g.,

Scholz, 1998; Rubin & Ampuero, 2005). Both aseismic slips and fluid movements may have contributed to the occurrence of foreshock activity.

Physical simulations indicate that interseismic creep penetrates seismogeneic patches from external stable-slip regions before the occurrence of unstable slip in the seismogeneic patches (Tse & Rice, 1986). Such an expansion of quasi-static slip prior to the mainshock may explain the currently observed migration behaviors in the foreshock activity (e.g., Dodge et al., 1996; Yabe & Ide, 2018). The source size of the mainshock rupture, however, is smaller than the range of foreshock occurrences, such that the aftershocks also migrate upward using several planes, which can be appropriately explained by the pore pressure migration model in a consistent manner. Thus, we prefer the hypothesis that states that the combined effects of pore pressure migration and triggered aseismic slip are responsible for generating the 2017 M5.3 Kagoshima Bay earthquake sequence.

4.2. Upward migration of the aftershock activity along several planes

Overall, we find that the aftershock hypocenters migrated toward the shallower portion using several planes, which were dipping steeply to the east. Previous studies have also reported such upward movements in the hypocenters for several earthquake swarms in northeastern Japan induced by the M9.0 Tohoku-Oki earthquake (Okada et al., 2015; Yoshida & Hasegawa, 2018a,b). As these upward movements occurred in the stress shadow of the 2011 Tohoku-Oki earthquake, these studies estimate the cause as upward pore pressure migration after the 2011 Tohoku-Oki earthquake (Terakawa et al., 2013; Yoshida et al., 2016a). The upward migration of aftershocks within the present earthquake sequence can also be explained by the upward migration of pore pressure. Fluid paths in the crust may have expanded due to the deformation and shaking associated with the mainshock. This observation is similar to the prediction from the fault valve model proposed in Sibson (1992), where fluids discharge upward after the mainshock rupture.

Based on model simulations, Hainzl and Ogata (2005) point out that the background seismicity rate of the ETAS model is sensitive to the amount of injected water. Pore pressure migration may explain deviations in the seismicity rate from Omori's law in terms of the present earthquake. Previous studies have obtained similar observations for fluid-injection-induced seismicity and natural earthquake sequences (Llenos & Michael, 2013; Yoshida & Hasegawa, 2018b; Kumazawa et al., 2019). Hypocenters rapidly migrate upward during this period (Fig. S7), supporting this hypothesis.

4.3. Comprehensive interpretation of the seismic activity in Kagoshima Bay

Here, we propose a simple model that comprehensively explains the observed results of the foreshock-mainshock-aftershock sequence of the 2017 M5.3 Kagoshima Bay earthquake. First, the foreshock activity represents the occurrence of small earthquakes caused by fluids that have infiltrated the mainshock fault plane. We presume that the subducting slab is the source of fluids, similar to the model reported in Hasegawa et al. (2005). The hypocenter migration of the foreshock activity can be interpreted as a reflection of fluid movement and possibly triggered aseismic slips on the plane.

Second, the seismic gap in the foreshock activity originates from the spatial heterogeneities in the frictional and material properties along the fault plane. The fault strength of the mainshock rupture area may have been higher than that of the surrounding area, as proposed in the asperity model of Lay & Kanamori (1981). Alternatively, the area may have

been covered by an impermeable medium, such that fluid intrusion was difficult. Foreshocks activities can be understood based on the failures of small seismogenic patches in the surrounding area. The occurrence of foreshocks and possible aseismic slips increases the shear stress at the future source region of the mainshock rupture. The mainshock rupture finally occurred in this region due to the gradually increasing pore pressure and shear stress.

Third, the change in stress associated with the occurrence of the mainshock primarily triggered the aftershocks in the area surrounding the mainshock rupture, including areas outside the mainshock fault plane. Fluids also began to move upward due to the deformation and shaking associated with the mainshock rupture. Together with the fluids, the aftershock hypocenters moved from deep to shallow portions.

Thus, the overall sequence of the 2017 M5.3 Kagoshima Bay earthquake can be appropriately explained by upward fluid movement, as presumed by the fault-valve model of Sibson (1992).

5. Conclusions

We relocated the hypocenters of the earthquake sequence of the 2017 M5.3 Kagoshima Bay earthquake based on the Double-Difference method (Waldhauser & Ellsworth, 2000) using numerous and precise differential arrival time data. Relocated hypocenters show that most earthquakes occurred on several planes. The orientations of those in the nodal planes of the focal mechanisms for individual earthquakes are nearly parallel to those macroscopic planes in the hypocenters, suggesting that these individual earthquakes occurred due to slip on several of these planar structures.

Most foreshocks were located on a single plane steeply dipping to the east, with migration along the plane. The observed speed and spatial pattern of hypocenter migration were consistent with the pore pressure diffusion model (D_h = 0.01–10 m^2/s ; e.g., Talwani et al. 2007; Shelly et al., 2016; Yoshida & Hasegawa, 2018a). This suggests that fluid movement caused foreshock activity and its migration behavior. Aseismic slip may have also been triggered by an increase in the pore pressure and contributed to the foreshock occurrence.

Foreshocks hypocenters clearly formed a seismic gap in the middle of the foreshock distribution, where the aftershock seismicity also appears to avoid this gap. The mainshock hypocenter was located along an edge of this seismic gap. Furthermore, the source size of the mainshock rupture estimated by the circular crack model was approximately the same as that of the seismic gap. This suggests that the mainshock rupture was due to the slip of this seismic gap. The seismic gap may be a large seismogenic patch with a relatively higher fault strength, which finally ruptured due to pore pressure migration and possible aseismic slip in the surrounding areas.

Aftershocks occurred on several planes, most of which have a steep incline to the east, and moved, as a whole, from deeper to shallower portions. This can be explained by upward fluid movement along all of the inclined planes after the mainshock. The overall sequence of the 2017 M5.3 Kagoshima Bay earthquake can be appropriately explained by upward fluid movement, as presumed by the fault-valve model proposed in Sibson (1992).

Acknowledgments

This study used hypocenter and P- and S-wave arrival time data reported in the unified catalog of the JMA (https://www.data.jma.go.jp/svd/eqev/data/bulletin/index_e.html). The seismograms were collected and stored by the JMA, national universities, and National Research Institute for Earth Science and Disaster Resilience (http://www.hinet.bosai.go.jp/?LANG=en). The figures in this paper were created using GMT (Wessel & Smith, 1998). This research was supported by JSPS KAKENHI Grant Number JP 17K1437. The obtained results for the hypocenters, focal mechanisms, and coseismic slip distribution are available at http://www.aob.gp.tohoku.ac.jp/~yoshida/pub/JGR2020b/.

References

Aki, K. (1965). A computer program for precise determination of focal mechanism of local earthquakes by revising focal depths and crust-mantle structure. Bull. Earthq. Res. Inst, 43, 15–22.

Aki, K. (1967). Scaling law of seismic spectrum. Journal of Geophysical Research, 72(4), 1217–1231.

Asano, Y., Saito, T., Ito, Y., Shiomi, K., Hirose, H., Matsumoto, T., et al. (2011). Spatial distribution and focal mechanisms of aftershocks of the 2011 off the Pacific coast of Tohoku Earthquake. Earth, Planets and Space, 63(7), 29.

Cornet, F. H., Helm, J., Poitrenaud, H., & Etchecopar, A. (1997). Seismic and aseismic slips induced by large-scale fluid injections. In Seismicity associated with mines, reservoirs and fluid injections (pp. 563–583). Springer.

Cox, S. F. (2016). Injection-driven swarm seismicity and permeability enhancement: Implications for the dynamics of hydrothermal ore systems in high fluid-flux, overpressured faulting regimes—An invited paper. Economic Geology, 111(3), 559–587.

Dahm, T. (1996). Relative moment tensor inversion based on ray theory: theory and synthetic tests. Geophysical Journal International, 124(1), 245–257.

Das, S., & Henry, C. (2003). Spatial relation between main earthquake slip and its aftershock distribution. Reviews of Geophysics, 41(3).

De Barros, L., Cappa, F., Deschamps, A., & Dublanchet, P. (2020). Imbricated Aseismic Slip And Fluid Diffusion Drive A Seismic Swarm In The Corinth Gulf, Greece. Geophysical Research Letters.

Dodge, D. A., Beroza, G. C., & Ellsworth, W. L. (1996). Detailed observations of California foreshock sequences: Implications for the earthquake initiation process. Journal of Geophysical Research: Solid Earth, 101(B10), 22371–22392.

Ebel, J. E., & Chambers, D. W. (2016). Using the locations of M≥ 4 earthquakes to delineate the extents of the ruptures of past major earthquakes. Geophysical Supplements to the Monthly Notices of the Royal Astronomical Society, 207(2), 862–875.

Ellsworth, W. L. (2013). Injection-induced earthquakes. Science, 341(6142), 1225942.

Guglielmi, Y., Cappa, F., Avouac, J.-P., Henry, P., & Elsworth, D. (2015). Seismicity triggered by fluid injection--induced aseismic slip. Science, 348(6240), 1224–1226.

Gutenberg, B., & Richter, C. F. (1944). Frequency of earthquakes in California. Bulletin of the Seismological Society of America, 34(4), 185–188.

Hainzl, S., & Ogata, Y. (2005). Detecting fluid signals in seismicity data through statistical earthquake modeling. Journal of Geophysical Research: Solid Earth, 110(5), 1–10. https://doi.org/10.1029/2004JB003247

Hasegawa, A. (2017). Role of H2O in Generating Subduction Zone Earthquakes. Monographs on Environment, Earth and Planets, 5(1), 1–34. https://doi.org/10.5047/meep.2017.00501.0001

Hasegawa, A., Nakajima, J., Umino, N., & Miura, S. (2005). Deep structure of the northeastern Japan arc and its implications for crustal deformation and shallow seismic activity. Tectonophysics, 403(1–4), 59–75. https://doi.org/10.1016/j.tecto.2005.03.018

Hubbert, M. K., & Rubey, W. W. (1959). Role of fluid overpressure in the mechanics of overthrust faulting. Geological Society of America Bulletin, 70, 167–206. https://doi.org/10.1130/0016-7606(1959)70

Kato, A., Fukuda, J., Nakagawa, S., & Obara, K. (2016). Foreshock migration preceding the 2016 Mw 7.0 Kumamoto earthquake, Japan. Geophysical Research Letters, 43(17), 8945–8953. https://doi.org/10.1002/2016GL070079

Kumazawa, T., & Ogata, Y. (2013). Quantitative description of induced seismic activity before and after the 2011 Tohoku-Oki earthquake by nonstationary ETAS models. Journal of Geophysical Research: Solid Earth, 118(12), 6165–6182.

Kumazawa, T., Ogata, Y., & Tsuruoka, H. (2019). Characteristics of seismic activity before and after the 2018 M6. 7 Hokkaido Eastern Iburi earthquake. Earth, Planets and Space, 71(1), 1–17.

Lay, T., & Kanamori, H. (1981). An asperity model of large earthquake sequences. In Earthquake Prediction. Maurice Ewing Series (pp. 579–592). American Geophysical Union.

Llenos, A. L., & Michael, A. J. (2013). Modeling earthquake rate changes in Oklahoma and Arkansas: Possible Signatures of induced seismicity. Bulletin of the Seismological Society of America, 103(5), 2850–2861. https://doi.org/10.1785/0120130017

Lohman, R. B., & McGuire, J. J. (2007). Earthquake swarms driven by aseismic creep in the Salton Trough, California. Journal of Geophysical Research: Solid Earth. https://doi.org/10.1029/2006JB004596

Madariaga, B. Y. R. (1976). Dynamics of an expanding circular fault. Bulletin of the Seismological Society of America, 66, 639–666. https://doi.org/10.1111/j.1461-0248.2009.01352.x

Mendoza, C., & Hartzell, S. H. (1988). Aftershock patterns and main shock faulting. Bulletin of the Seismological Society of America, 78(4), 1438–1449.

Nanjo, K. Z., Miyaoka, K., Tamaribuchi, K., Kobayashi, A., & Yoshida, A. (2018). Related spatio-temporal changes in hypocenters and the b value in the 2017 Kagoshima Bay swarm activity indicating a rise of hot fluids. Tectonophysics, 749, 35–45.

Nur, A., & Booker, J. R. (1972). Aftershocks caused by pore fluid flow? Science, 175(4024), 885–887. https://doi.org/10.1126/science.175.4024.885

Ogata, Y. (2006). Statistical analysis of seismicity: updated version (SASeis2006). Institute of Statistical Mathematics.

Ogata, Y. (1988). Statistical models for earthquake occurrences and residual analysis for point processes. Journal of the American Statistical Association, 83(401), 9–27.

Okada, T., Matsuzawa, T., Umino, N., Yoshida, K., Hasegawa, A., Takahashi, H., et al. (2016). Hypocenter migration and crustal seismic velocity distribution observed for the inland earthquake swarms induced by the 2011 Tohoku-Oki earthquake in NE Japan: Implications for crustal fluid distribution and crustal permeability. In Crustal Permeability (pp. 307–323). https://doi.org/10.1002/9781119166573.ch24

Rice, J. R. (1992). Fault stress states, pore pressure distributions, and the weakness of the San Andreas fault. In International geophysics (Vol. 51, pp. 475–503). Elsevier.

Roland, E., & McGuire, J. J. (2009). Earthquake swarms on transform faults. Geophysical Journal International, 178(3), 1677–1690. https://doi.org/10.1111/j.1365-246X.2009.04214.x

Ross, Z. E., Kanamori, H., & Hauksson, E. (2017). Anomalously large complete stress drop during the 2016 Mw5.2 Borrego Springs earthquake inferred by waveform modeling and near-source aftershock deficit. Geophysical Research Letters, 44(12), 5994–6001. https://doi.org/10.1002/2017GL073338

Ross, Z. E., Kanamori, H., Hauksson, E., & Aso, N. (2018). Dissipative Intraplate Faulting During the 2016 Mw6.2 Tottori, Japan Earthquake. Journal of Geophysical Research: Solid Earth, 123(2), 1631–1642. https://doi.org/10.1002/2017JB015077

Ross, Z. E., Rollins, C., Cochran, E. S., Hauksson, E., Avouac, J. P., & Ben-Zion, Y. (2017). Aftershocks driven by afterslip and fluid pressure sweeping through a fault-fracture mesh. Geophysical Research Letters, 44(16), 8260–8267. https://doi.org/10.1002/2017GL074634

Saiga, A., Matsumoto, S., Uehira, K., Matsushima, T., & Shimizu, H. (2010). Velocity structure in the crust beneath the Kyushu area. Earth, Planets and Space, 62(5), 449–462.

Sato, T., & Hirasawa, T. (1973). Body wave spectra from propagating shear cracks. Journal of Physics of the Earth, 21(4), 415–431. https://doi.org/10.4294/jpe1952.21.415

Scholz, C. H. (1998). Earthquakes and friction laws. Nature, 391(6662), 37–42. https://doi.org/10.1038/34097

Shapiro, S. A., Huenges, E., & Borm, G. (1997). Estimating the crust permeability from fluid-injection-induced seismic emission at the KTB site. Geophysical Journal International, 131(2). https://doi.org/10.1111/j.1365-246X.1997.tb01215.x

Shelly, D. R., Ellsworth, W. L., & Hill, D. P. (2016). Fluid-faulting evolution in high definition: Connecting fault structure and frequency-magnitude variations during the 2014 Long Valley Caldera, California, earthquake swarm. Journal of Geophysical Research : Solid Earth, 121, 1776–1795. https://doi.org/10.1002/2015JB012719.Received

Sibson, R. H. (2020). Preparation zones for large crustal earthquakes consequent on fault-valve action. Earth, Planets and Space, 72(1), 1–20.

Talwani, P., & Acree, S. (1985). Pore pressure diffusion and the mechanism of reservoir-induced seismicity. In Earthquake Prediction (pp. 947–965). Springer.

Talwani, P., Chen, L., & Gahalaut, K. (2007). Seismogenic permeability, ks. Journal of Geophysical Research: Solid Earth, 112(7), 1–18. https://doi.org/10.1029/2006JB004665

Terakawa, T., Hashimoto, C., & Matsu'ura, M. (2013). Changes in seismic activity following the 2011 Tohoku-oki earthquake: Effects of pore fluid pressure. Earth and Planetary Science Letters, 365, 17–24. https://doi.org/10.1016/j.epsl.2013.01.017

Ueno, H., Hatakeyama, S., Aketagawa, T., Funasaki, J., & Hamada, N. (2002). Improvement of hypocenter determination procedures in the Japan Meteorological Agency. Q. J. Seismol., 65, 123–134.

Utsu, T. (1961). A statistical study on the occurrence of aftershocks. Geophys. Mag., 30, 521–605.

Utsu, T., Ogata, Y., & Matsu'ura, R. (1995). The centenary of the Omori formula for a decay law of aftershock activity. Journal of Physics of the Earth, 43(1), 1–33.

Vidale, J. E., Boyle, K. L., & Shearer, P. M. (2006). Crustal earthquake bursts in California and Japan: Their patterns and relation to volcanoes. Geophysical Research Letters, 33(20), 1–5. https://doi.org/10.1029/2006GL027723

Waite, G. P., & Smith, R. B. (2002). Seismic evidence for fluid migration accompanying subsidence of the Yellowstone caldera. Journal of Geophysical Research: Solid Earth, 107(B9), ESE--1.

Waldhauser, F. (2002). Fault structure and mechanics of the Hayward Fault, California, from double-difference earthquake locations. Journal of Geophysical Research, 107(B3), 2054. https://doi.org/10.1029/2000JB000084

Wetzler, N., Lay, T., Brodsky, E. E., & Kanamori, H. (2018). Systematic deficiency of aftershocks in areas of high coseismic slip for large subduction zone earthquakes. Science Advances, 4(2), 1–10. https://doi.org/10.1126/sciadv.aao3225

Woessner, J., Schorlemmer, D., Wiemer, S., & Mai, P. M. (2006). Spatial correlation of aftershock locations and on-fault main shock properties. Journal of Geophysical Research: Solid Earth, 111(B8).

Yabe, S., & Ide, S. (2018). Variations in precursory slip behavior resulting from frictional heterogeneity. Progress in Earth and Planetary Science, 5(1), 43.

Yoshida, K., & Hasegawa, A. (2018a). Sendai-Okura earthquake swarm induced by the 2011 Tohoku-Oki earthquake in the stress shadow of NE Japan: Detailed fault structure and hypocenter migration. Tectonophysics, 733(August 2017), 132–147. https://doi.org/10.1016/j.tecto.2017.12.031

Yoshida, K., & Hasegawa, A. (2018b). Hypocenter Migration and Seismicity Pattern Change in the Yamagata-Fukushima Border, NE Japan, Caused by Fluid Movement and Pore Pressure Variation. Journal of Geophysical Research: Solid Earth, 123(6), 5000–5017. https://doi.org/10.1029/2018JB015468

Yoshida, K., Hasegawa, A., & Okada, T. (2016a). Heterogeneous stress field in the source area of the 2003 M6.4 Northern Miyagi Prefecture, NE Japan, earthquake. Geophysical Journal International, 206(1), 408–419. https://doi.org/10.1093/gji/ggw160

Yoshida, K., Hasegawa, A., & Yoshida, T. (2016b). Temporal variation of frictional strength in an earthquake swarm in NE Japan caused by fluid migration. Journal of Geophysical Research: Solid Earth, 121(8), 5953–5965. https://doi.org/10.1002/2016JB013022

Yoshida, K., Hasegawa, A., Yoshida, T., & Matsuzawa, T. (2019a). Heterogeneities in stress and strength in tohoku and its relationship with earthquake sequences triggered by the 2011 M9 Tohoku-Oki earthquake. Pure and Applied Geophysics, 176(3), 1335–1355.

Yoshida, K., Saito, T., Emoto, K., Urata, Y., & Sato3, D. (2019b). Rupture directivity, stress drop, and hypocenter migration of small- and moderate-sized earthquakes in the Yamagata-Fukushima border swarm triggered by upward pore-pressure migration after the 2011 Tohoku-Oki earthquake. Tectonophysics, 769, 228184.

Yoshida, K., Taira, T., Matsumoto, Y., Saito, T., Emoto, K., & Matsuzawa, T. (n.d.). Stress release process along an intraplate fault analogous to the plate boundary: a case study of the 2017 M5. 2 Akita-Daisen earthquake, NE Japan. Journal of Geophysical Research: Solid Earth, e2020JB019527.

Yukutake, Y., Ito, H., Honda, R., Harada, M., Tanada, T., & Yoshida, A. (2011). Fluid-induced swarm earthquake sequence revealed by precisely determined hypocenters and focal mechanisms in the 2009 activity at Hakone volcano, Japan. Journal of Geophysical Research: Solid Earth, 116(4). https://doi.org/10.1029/2010JB008036